Nanoscale

ROYAL SOCIETY OF CHEMISTRY

PAPER

View Article Online
View Journal | View Issue

Cite this: *Nanoscale*, 2026, **18**, 9650

Conformation-induced Kondo switch of fluorenyl radicals on a metal surface through adsorption

Jia Liu,†[a,b] Yanbo Li,†[a,b] Jianmin Huang,[a,b] Shijing Tan,[a,b] Chuanxu Ma,[a,b] Qitang Fan*[a,b] and Bing Wang*[a,b]

Received 1st February 2026,
Accepted 30th March 2026

DOI: 10.1039/d6nr00433d

rsc.li/nanoscale

Controlling whether a molecular radical retains its spin on a metal surface is a key prerequisite for building switchable, atomically precise carbon-based spin architectures. Here, we use 3,6-bis(4-bromophenyl)-9*H*-fluorene to synthesize covalently linked fluorene trimers and oligomeric chains on Au(111) *via* Ullmann coupling and then generate strongly localized fluorenyl-type radical centers by site-selective tip-induced dehydrogenation. Combining the bond-resolved nc-AFM with scanning tunneling spectroscopy, we identify two interconvertible adsorption configurations: a non-bonded radical state that displays a pronounced zero-bias Kondo resonance and a chemisorbed state in which a local C–Au bond is formed at the radical site, accompanied by a characteristic geometric relaxation of the five-membered ring and complete quenching of the Kondo resonance. In both the macrocycles and chains, the distribution of the Kondo-active sites depends on metastable global adsorption geometries and can be reversibly reconfigured by tip perturbation. These results establish a structure-resolved chemisorption *versus* physisorption switch as a practical design rule for stabilizing and toggling spins in multi-radical rings and chains directly on metallic substrates, opening opportunities for programmable quantum spin functionalities in surface-supported π-systems.

Introduction

Atomically precise control of spins in surface-supported π-systems has become a central route toward designer quantum magnets,[1–3] spin chains[4–12] and spin rings.[13–15] On-surface synthesis has enabled magnetic nanographenes[16–18] whose spin states are encoded by sublattice imbalance or topological frustration,[19] and then assembled into coupled architectures with controllable length, parity and exchange topology. Clar's goblet is a representative building block in this context. Its unconventional magnetism originates from topological frustration, and its covalent linking has been exploited to realize well-defined Heisenberg chains with tunable terminations and excitations.[4,6,19,20] Complementary strategies using other open-shell nanographenes, such as triangulenes, further demonstrate that purely carbon frameworks can host spin-1/2 chains and engineered excitations when the local moments remain intact upon adsorption.[4,6,7,10]

A persistent practical constraint is that the presence of a molecular radical motif does not automatically guarantee a visible local moment on a metal.[19,20] The decisive factor is the local degree of hybridization with the substrate, which ranges from weak adsorption that still permits a local magnetic moment and allows Kondo screening to chemisorption that quenches the local moment through bond formation and strong charge redistribution. Tip-induced chemistry has emerged as a powerful way to program spins at the single-bond level, including site-selective dehydrogenation that can either create an unpaired electron or eliminate it when a metal–carbon bond is formed at the activated site.[20] A related control over molecular spin states has also been demonstrated for Clar's goblet on Au(111), where the formation or breaking of a C–Au bond at specific adsorption sites switches the system between the $S = 1/2$ and $S = 0$ states. However, such switching relies on site-specific chemisorption configurations imposed by the substrate, rather than an intrinsic, geometry-defined adsorption degree of freedom of the molecule itself.[19] Despite this progress, direct real-space identification of a geometry-defined chemisorption channel that toggles a radical spin on Au(111), with simultaneous structural assignment and spectroscopic verification, remains scarce.[21,22]

Fluorenyl radicals provide an attractive testbed because their spin density is highly localized and chemically well defined. In electronically decoupled environments, such as

---

[a] Hefei National Research Center for Physical Sciences at the Microscale, CAS Center for Excellence in Quantum Information and Quantum Physics, and New Cornerstone Science Laboratory, University of Science and Technology of China, Hefei, Anhui 230026, China. E-mail: qtfan@ustc.edu.cn, bwang@ustc.edu.cn
[b] Hefei National Laboratory, University of Science and Technology of China, Hefei 230088, China

† These authors contributed equally to this work.

molecules prepared and probed on thin insulating NaCl films, fluorenyl-type open-shell motifs and closely related indenofluorene derivatives show stable spin states and adsorption-site-dependent switching between open- and closed-shell configurations.[23,24] These results establish fluorene-derived radicals as robust molecular spin centers when direct hybridization with metal states is suppressed, and they highlight adsorption geometry as an effective control knob.

Here, we extend this concept to a fully metallic environment and identify a geometry-controlled quenching pathway that is specific to a fluorenyl-type radical on Au(111). Using 3,6-bis(4-bromophenyl)-9*H*-fluorene (BPF, Scheme 1) as a precursor, Ullmann coupling on Au(111) yields covalently linked fluorene trimers in both the cyclic trimer and chain-like motifs, as illustrated in Scheme 1 (step 1). Because thermal dehydrogenation on Au(111) promotes undesired intermolecular coupling, we generate radical CH centers by site-specific tip pulses (Scheme 1, step 2). The combined non-contract atomic force microscopy (nc-AFM) and scanning tunnelling spectroscopy (STS) resolve two interconvertible adsorption configurations: a non-bonded radical state that exhibits a pronounced Kondo resonance, and a chemisorbed state in which a local C–Au bond forms at the radical site, accompanied by a characteristic geometric relaxation (tilt/approach of the five-membered ring) and a complete suppression of the Kondo feature. These observations provide direct, structure-resolved evidence that, on Au(111), the expression of a fluorenyl-type spin moment is governed by adsorption geometry through a chemisorption *versus* physisorption switch at the radical site. This chemisorption-controlled Kondo on/off behavior establishes a practical design rule for multi-spin rings and chains on metals and offers a route to switchable spin functionality by controlling local adsorption configurations.

Results and discussion

The BPF monomer was synthesized in solution *via* a two-step reaction as described in detail in the SI Methods and SI Fig. S1. After the thermal deposition of BPF onto Au(111) and held at 300 K, chain-like supramolecular assemblies composed of periodically linked square motifs were observed (Fig. 1a). A magnified STM image (Fig. 1b) shows that each square is formed by two bent molecules, which connect an adjacent square by intermolecular halogen and hydrogen bonds. The corresponding bond-resolved nc-AFM image (Fig. 1c) identifies

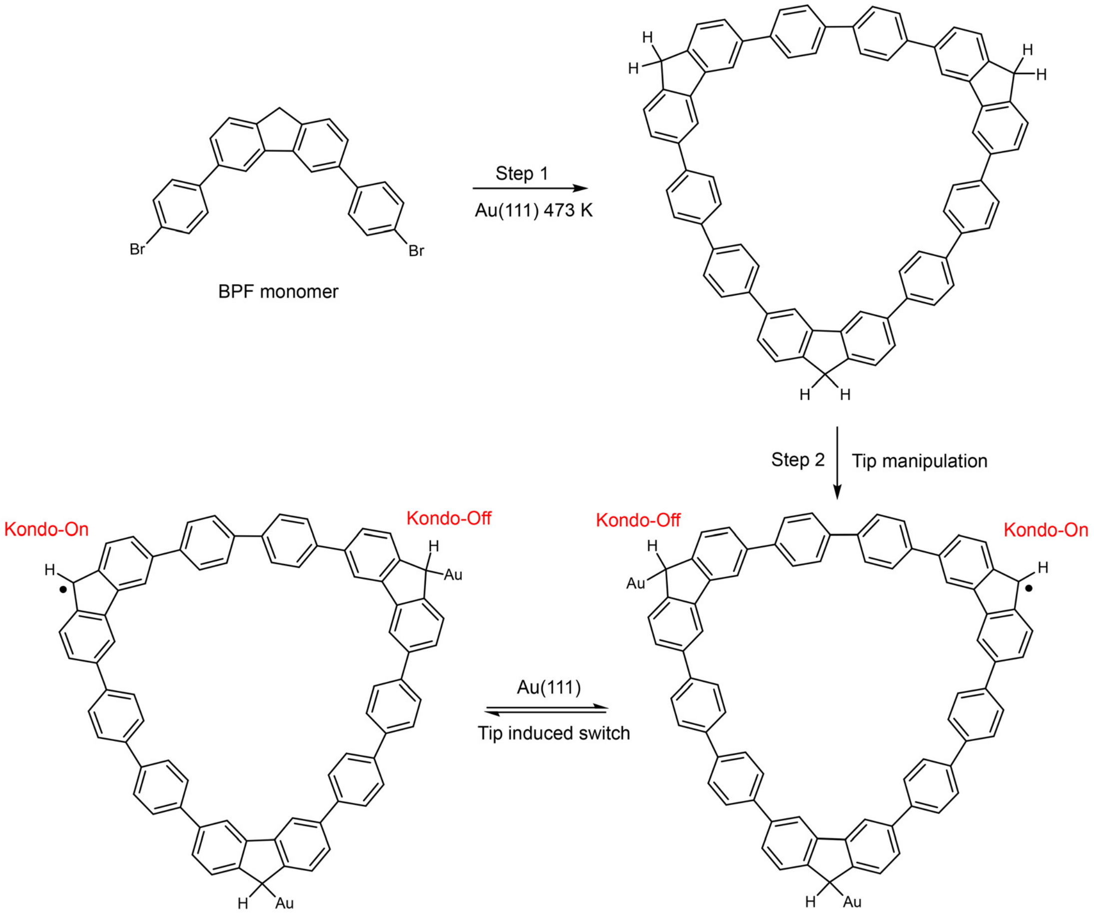

Scheme 1 Schematic of the on-surface synthesis and tip-induced generation of fluorenyl-type radical sites in the trimer macrocycle on Au(111).

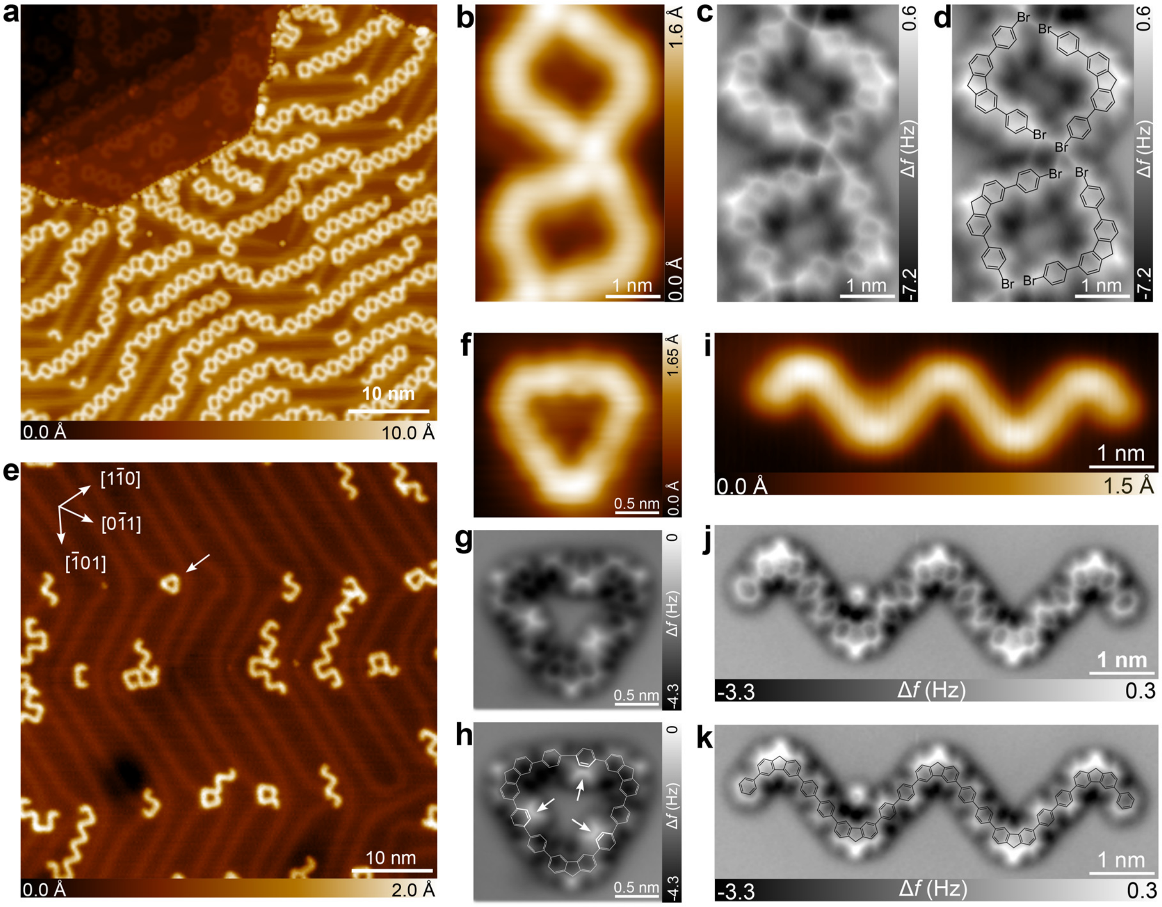

Fig. 1 Adsorption and reaction of BPF on Au(111). (a) Large-scale STM image of self-assemblies after the deposition of BPF molecules on Au(111) at 150 °C. (b–d) Zoom-in STM (b), nc-AFM (c) image and the corresponding derived chemical structure (d) of a section of a typical assembly structural motif. (e) Overview STM image taken after annealing the sample in panel (a) to 473 K. (f–h) Magnified STM (f), nc-AFM (g) images, and the corresponding overlaid chemical structure (h) of a covalent trimer macrocycle. (i–k) Magnified STM (i), nc-AFM (j) images, and superimposed chemical structure (k) of a covalent oligomeric chain (V = −15 mV, I = 50 pA, and ΔZ = 0.4 Å). Tunneling parameters: (a and b) U = −1 V and I = 20 pA; (f and i) U = −0.5 V and I = 20 pA. The nc-AFM images were recorded using a CO-functionalized tip at a height ΔZ of 20 pm (c) and 40 pm (g and j) with respect to the STM setpoint: U = −15 mV and I = 50 pA.

these building blocks as intact BPF molecules bearing two terminal C–Br groups, as shown by Fig. 1d. The supramolecular stabilization is consistent with halogen-bonding interactions among Br substituents (Br⋯Br), together with additional Br⋯H contacts, as commonly reported for halogenated arenes on coinage-metal surfaces.[25–27]

Upon annealing the sample to 473 K, BPF undergoes debromination followed by C–C coupling, yielding predominantly zigzag-shaped oligomeric chains and, less frequently, trimeric macrocycles adsorbed with their straight sides along the close-packed directions of Au(111) (Fig. 1e, white arrows). The zoomed-in STM and nc-AFM images of a representative macrocycle (Fig. 1f and g) reveal a covalent trimer consisting of three coupled 3,6-bisphenyl-9*H*-fluorene moieties as illustrated by the overlaid chemical structure in Fig. 1h. Notably, the three peripheral phenylene units (marked by white arrows in Fig. 1h) appear tilted upward, which we attribute to steric repulsion between adjacent C–H groups at the coupling junctions. In contrast, the methylene ($-CH_2-$) groups in the five-membered rings remain intact at this stage, exhibiting a distinctly brighter contrast in nc-AFM, indicating that dehydrogenation of ($-CH_2-$) to –CH– has not yet occurred.

A representative linear oligomer shows an analogous situation (Fig. 1i and j). The STM image resolves a chain consisting of five 3,6-bisphenyl-9*H*-fluorene units, with an increased apparent height at the "corner" positions associated with the ($-CH_2-$) containing five-membered rings. Consistently, the corresponding nc-AFM image shows brighter contrast at these corners, again supporting intact ($-CH_2-$) groups. We also observe an upward tilting of phenylene units in the zigzag backbone. Compared to the macrocycle, the tilting is weaker, which we attribute to additional strain in the macrocycle: the natural angle imposed by the BPF substitution pattern is less compatible with a 60° cyclization geometry, leading to increased distortion in the trimeric ring.

To generate fluorenyl-type radicals by thermal activation, we annealed the sample (Fig. 1e) to 623 K, aiming to dehydrogenate the ($-CH_2-$) groups in the five-membered rings.

However, as shown in SI Fig. S2, the oligomers transform into laterally coupled two-dimensional network patches. This behavior indicates that (–CH_2–) dehydrogenation can indeed occur on Au(111), but the resulting radical intermediates are rapidly trapped by intermolecular C–C bond formation. Consequently, purely thermal activation does not provide a viable route to isolated fluorenyl radicals on Au(111) in our system.

We therefore employed tip-induced manipulation to remove hydrogen atoms from the (–CH_2–) groups in a controlled, site-selective manner. As illustrated in Fig. 2a, the tip was positioned above a selected corner of the trimer macrocycle (white arrow), and a voltage pulse of around 2.8 V and current of 2–3 nA was applied. After a duration ranging at 2–3 s, a downward current step was typically observed (SI Fig. S3), consistent with a manipulation event assigned to the removal of a single H atom from the methylene group ($CH_2 \rightarrow CH$). After manipulation, the targeted corner exhibits a markedly reduced apparent height in STM (Fig. 2a) and a darker contrast in the nc-AFM image (Fig. 2b), which is attributed to the bonding of the CH group to the substrate gold atom illustrated by the chemical structure in Fig. 2d. The corresponding constant-height current map (Fig. 2c) shows an enhanced electronic signal around the manipulated site, consistent with the formation of a modified local electronic structure. Applying the same procedure to the remaining corners produces a fully manipulated trimer macrocycle, in which all three (–CH_2–) groups are converted into CH centers (Fig. 2e–l), which bond to the lattice gold atom. Immediately after the third manipulation, the nc-AFM imaging often shows signs of instability (frequency-shift signal "jumps"; Fig. 2j), indicating that the adsorption geometry is metastable and can relax under continued scanning.

After several imaging scans, the fully manipulated trimer macrocycle relaxes into a more stable adsorption configuration (Fig. 3a). In this state, two corners (marked by blue and green arrows) display a truncated appearance at the pentagon site, while one corner (marked by a red arrow) remains bright. We interpret the dark corners as fluorenyl-type centers that have formed a local C–Au bond at the CH site, leading to a local geometric relaxation, in which the five-membered ring approaches the substrate. Conversely, the bright corner corresponds to a non-bonded radical center that retains its localized moment.

This assignment is directly supported by bond-resolved nc-AFM data recorded at the same nominal tip height for the three corners (Fig. 3c, e and f). At the dark corners (Fig. 3c and f), the two benzene rings of the fluorene unit are clearly resolved, whereas the five-membered ring is not visible at this imaging height. Importantly, when the tip is approached by an additional 100 pm (Fig. 3d and g), the five-membered ring becomes detectable, demonstrating that it is not chemically missing but rather displaced toward the surface, consistent

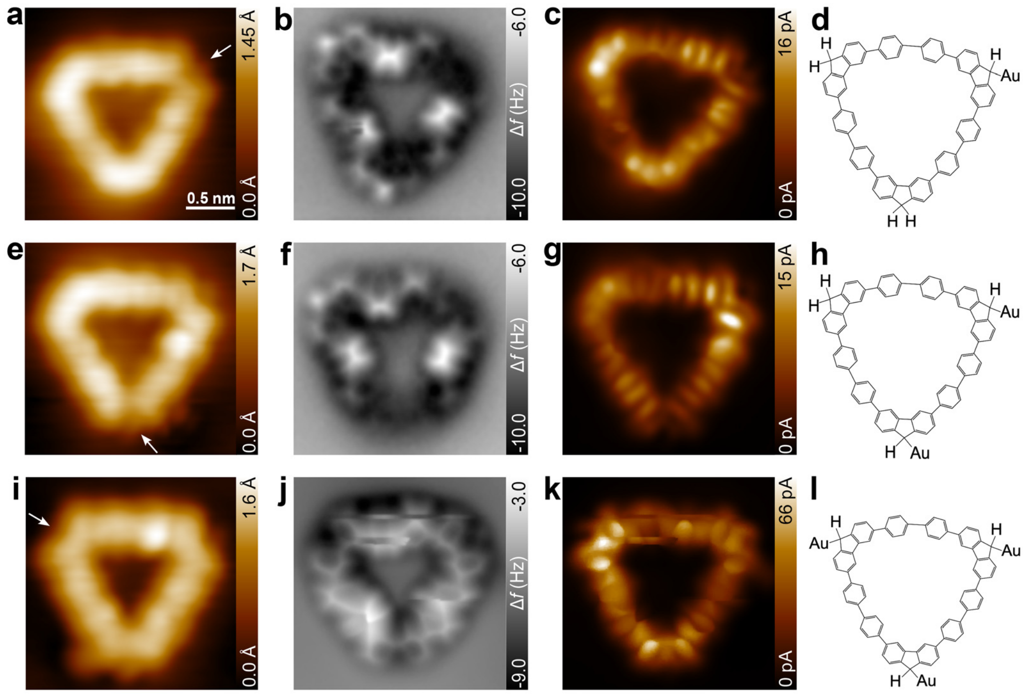

Fig. 2 Tip-induced stepwise H removal on the trimer macrocycle. (a–d) STM topography (a), constant-height nc-AFM (b), current map (c), and structural model (d) after the first H removal at the arrow-marked corner. (e–h) Same as (a–d) after the second H removal at the arrow-marked corner in (e). (i–l) Same as (a–d) after the third H removal at the arrow-marked corner in (i). Parameters: STM (a, e and i) $U = -0.1$ V and $I = 20$ pA; nc-AFM (b) $U = -15$ mV, $I = 50$ pA, and $\Delta z = 35$ pm; (f) $U = -10$ mV, $I = 20$ pA, and $\Delta z = 30$ pm; (j) $U = -10$ mV, $I = 20$ pA, and $\Delta z = 0$ pm. Current maps (c, g and k) were acquired at 0 mV at the same tip height as (b, f and j), respectively. All the STM, nc-AFM images and current maps share the same scale bar in panel (a).

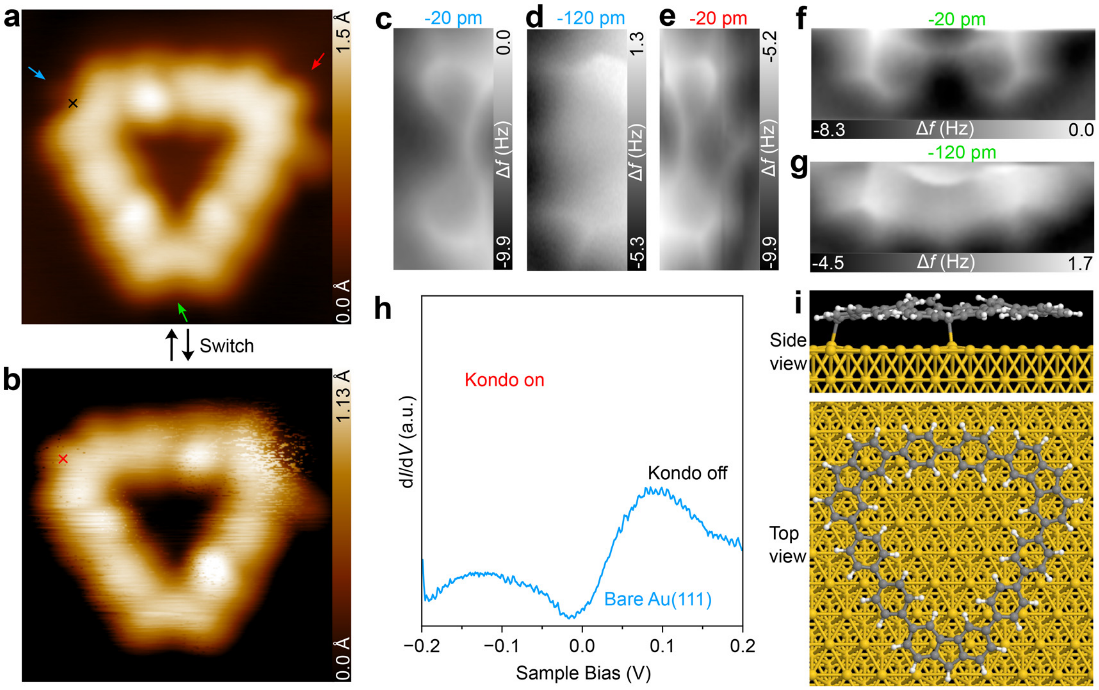

Fig. 3 Bonded *versus* non-bonded fluorenyl radicals in the trimer macrocycle. (a and b) Constant-current STM topographies showing two mirrored adsorption configurations of the trimer macrocycle after the removal of three H atoms. Dark corners are indicated by blue and green arrows, and the bright corner by the red arrow. (c and d) Bond-resolved constant-height nc-AFM images of the upper-left corner (blue arrow) acquired at $\Delta z = -20$ pm and -120 pm, respectively. (e) Bond-resolved constant-height nc-AFM image of the upper-right corner (red arrow) acquired at $\Delta z = -20$ pm. (f and g) Bond-resolved constant-height nc-AFM images of the bottom corner (green arrow) acquired at $\Delta z = -20$ pm and -120 pm, respectively. (h) dI/dV spectra acquired at the upper-left corner in (a) and (b), as marked by the black and red crosses, respectively. The blue curve shows the reference dI/dV spectra recorded on the bare Au(111) surface near the trimer macrocycle. (i) DFT-optimized adsorption configurations of the fully sp^2-hybridized trimer macrocycle on Au(111), featuring two fluorenyl-type radical sites bonded to the surface Au atoms and one non-bonded (Kondo-active) radical site. Parameters: STM (a, b) $U = -0.1$ V, $I = 20$ pA. All nc-AFM tip heights (c–g) are referenced to the STM setpoint $U = -10$ mV, $I = 20$ pA.

with the local chemisorption-induced tilting.[20,28,29] In contrast, at the bright corner (Fig. 3e), the full fluorene subunit, including the five-membered ring, is resolved already at the higher imaging height, consistent with a more flat non-bonded configuration. Spectroscopic measurements provide the corresponding electronic signature. The differential conductance (dI/dV) spectrum acquired at the red arrow-marked bright corner (Fig. 3h, red) shows a pronounced zero-bias peak assigned to a Kondo resonance, evidencing a surviving localized spin on Au(111). In contrast, spectra measured at the green arrow-marked dark corner (Fig. 3h, black) show no Kondo feature, consistent with moment quenching upon C–Au bond formation.

Notably, the adsorption state in Fig. 3a is metastable and can switch into a second configuration (Fig. 3b), in which the Kondo-active corner relocates from the upper-right to the upper-left position. After switching, the previously bright corner often appears blurred in STM, indicating residual structural metastability under tip perturbation. Continued scanning can drive the system back to the original configuration (Fig. 3c), suggesting two closely competing adsorption minima. DFT calculations (Fig. 3i) support this picture: for a fully sp^2 trimer macrocycle adsorbed with its sides along the high symmetry direction, two mirrored metastable configurations with identical adsorption energies of 7.97 eV are found, each featuring two chemisorbed (bonded) corners and one surviving radical corner. Switching between these mirrored states naturally explains the observed relocation of the Kondo-active site between the two equivalent corners. Moreover, the DFT calculation confirms the spin density distribution around the physisorbed fluorenyl radical sites, as shown by SI Fig. S4.

We performed analogous tip-induced dehydrogenation on a linear oligomeric chain to generate a multi-radical architecture on Au(111). The initial chain (Fig. 4a) contains five fluorene units with intact ($-CH_2-$) groups, evidenced by the bright nc-AFM contrast at the corner sites and the corresponding dI/dV maps at 0 mV. Voltage pulses applied at the selected corners convert the ($-CH_2-$) groups into CH centers in a controlled sequence. After converting four sites (Fig. 4b, red numbers), one corner (site "4") displays a bright contrast analogous to the Kondo-active corner in the macrocycle, together with a strongly enhanced 0 mV dI/dV signal. dI/dV spectroscopy at this site (Fig. 4e, black) reveals a clear zero-bias Kondo resonance, confirming the survival of a localized spin. In contrast, the remaining manipulated corners (sites 1, 3, and 5) show a darker contrast and weaker 0 mV current, consistent with chemisorption at the radical carbon and quenching of the moment.

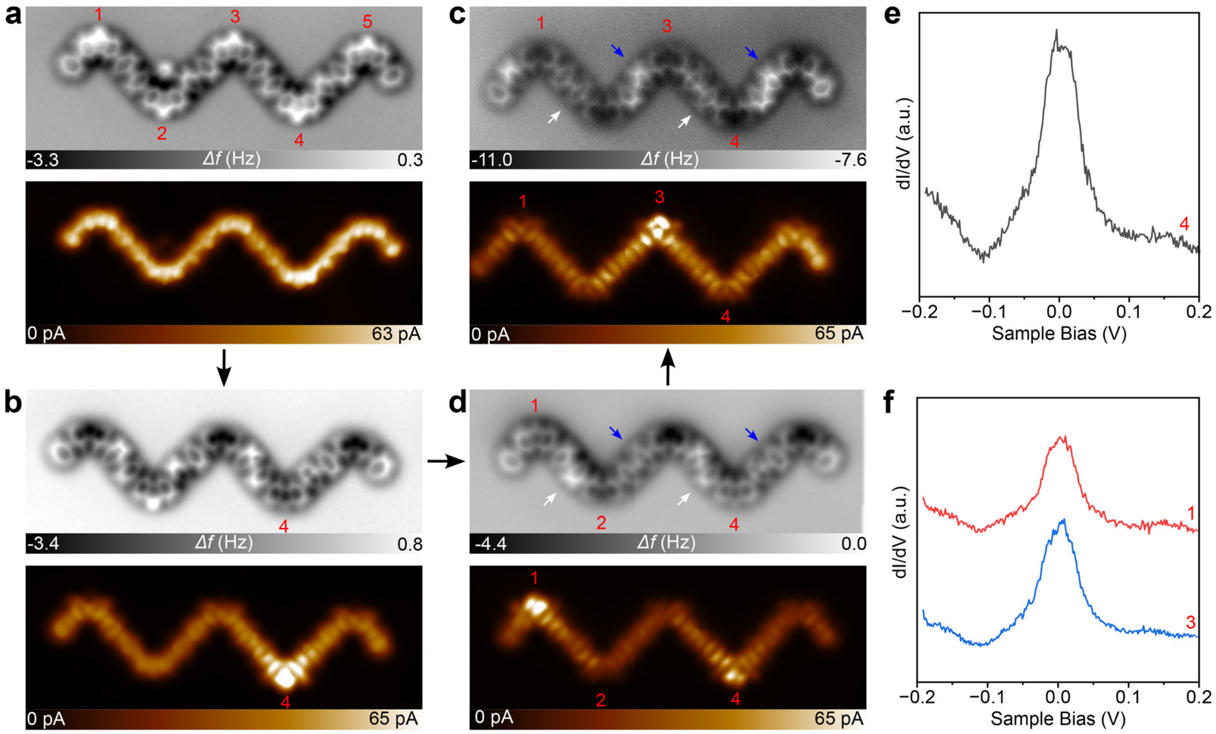

Fig. 4 Geometry-dependent Kondo on/off switching in a five-unit fluorenyl-radical chain on Au(111). (a) Constant-height nc-AFM image and simultaneously recorded current map of an oligomeric chain comprising five 3,6-bisphenyl-9*H*-fluorene moieties (all $(-CH_2-)$ intact). (b) Same as (a) after tip-induced H removal at the corner sites 1, 3, 4, and 5 (four $(-CH_2-) \rightarrow CH$ conversions). (d) Same as (a) after removing the remaining H atom at site 2 (all five sites converted), yielding an adsorption configuration in which sites 1 and 4 are Kondo-active. (c) Same as (a) after switching from the configuration in (d) induced by low tip-height scanning, resulting in a different metastable adsorption state. (e) d*I*/d*V* spectrum acquired at the corner site 4 in (b). (f) d*I*/d*V* spectra acquired at the corner site 1 in (d) (red) and at corner site 3 in (c) (blue). Parameters: nc-AFM images and current maps (a–d) were recorded at U = 0 mV at constant height (Δz = 0.3–0.1 Å) relative to the STM setpoint (U = –10 mV, I = 20 pA). Current maps were acquired simultaneously at 0 mV at the same tip height as the corresponding nc-AFM images.

After converting the final $(-CH_2-)$ site (site "2") to CH, the overall adsorption geometry of the chain can reorganize. In the configuration shown in Fig. 4d, site "4" remains Kondo-active as evidenced by the d*I*/d*V* spectrum in Fig. 4f (red line), while site "1" switches from a dark (Kondo-off) to a bright (Kondo-on) appearance in both the nc-AFM and the current map. Correspondingly, the d*I*/d*V* spectrum at site "1" (Fig. 4f, blue) develops a pronounced Kondo resonance. This behavior demonstrates that Kondo activity is not solely determined by the local chemical identity of an individual radical center, but can be toggled by a global adsorption rearrangement of the entire oligomer.

Further scanning at a reduced tip–sample distance (setpoint: 10 mV, 20 pA) induces additional switching into a different metastable adsorption state (Fig. 4c). In this new configuration, previously Kondo-active sites ("1" and "4") become Kondo-inactive, whereas a previously quenched site ("3") becomes Kondo-active. Simultaneously, the adsorption geometry of the phenylene backbone changes: phenylene units that were mutually tilted in Fig. 4b (white arrows) become flatter, while units that were initially flatter (blue arrows) adopt a more tilted configuration. These correlated structural and spectroscopic changes further establish the adsorption geometry, specifically, whether the radical carbon engages in local chemisorption with Au, as the governing factor behind the Kondo on/off state in the multi-radical chain.

Conclusion

In conclusion, we realized fluorenyl radicals in the on-surface-synthesized fluorene-containing macrocycles and oligomeric chains on Au(111) *via* site-selective tip-induced dehydrogenation, avoiding the uncontrolled intermolecular coupling that occurs during thermal activation. Bond-resolved nc-AFM imaging, together with STS, reveals a clear and local structural origin for the magnetic response: a fluorenyl radical exhibits a zero-bias Kondo resonance only when the radical carbon remains non-bonded to the substrate, whereas the formation of a local C–Au bond drives a distinct geometric relaxation of the five-membered ring and fully quenches the Kondo signature. Beyond identifying a single-site mechanism, we show that the Kondo-active sites in both the trimer macrocycle and the radical chain depend on the overall adsorption geometry and can switch between metastable configurations under tip perturbation. The resulting chemisorption/physisorption toggle at the individual radical centers provides a concrete, experimentally resolved design rule for carbon-based multi-spin architectures on metals: preserving local moments requires controlling adsorption configurations to prevent local chemisorption channels at the radical site. This insight should be broadly useful for constructing switchable spin chains and rings, and for engineering spatially programmable magnetic functionality in purely carbon frameworks directly on metallic substrates.

Methods

Sample preparation

Au(111) single crystals purchased from the MaTeck and Surface Preparation Laboratory (SPL) were used as substrates for the growth of the sample. The preparation of clean and well-defined Au(111) surfaces was achieved through cycles of Ar^+ ion bombardment and annealing at 850 K. The 3,6-bis(4-bromophenyl)-9*H*-fluorene (BPF) precursor was vapour-deposited (evaporator temperature of 300 K) onto a clean Au(111) surface held at room temperature, followed by post-annealing to 473 and 623 K for typically 15 min at each step to complete the reactions.

STM-AFM measurements

The STM and nc-AFM measurements were performed under ultra-high vacuum conditions (base pressure 1×10^{-10} mbar) with Scienta Omicron POLAR-STM/AFM combined systems operated at 4.5 K using a qPlus sensor equipped with a W tip. STM images were acquired in the constant-current mode at a sample temperature of 4.5 K. A sample bias with respect to the tip was used. For constant-height nc-AFM imaging, the tip was functionalized by controlled picking up of a single CO molecule at the tip apex from Ag(111), which enables imaging of the chemical structure of organic molecules.[30] The quartz cantilever (qPlus sensor) had a resonance frequency of $f_0 \approx 27\,000$ Hz, a quality factor of $Q \approx 50\,000$–$100\,000$ and was operated with an oscillation amplitude of $A_{\text{osc}} = 50$–70 pm and bias of 5 mV. This procedure was applied to all the nc-AFM images. Tip conditioning was performed by repeatedly bringing the tip into contact with the silver surface and applying bias pulses until the necessary STM resolution was achieved. The differential conductance (dI/dV) measurements were performed in the low-temperature STM/AFM at 4.5 K *via* the lock-in technique with a peak-to-peak bias-voltage modulation of 5 mV at a frequency of 973 Hz.

DFT calculations

All the calculations were performed using the Vienna *Ab initio* Simulation Package (VASP)[31,32] within the projector augmented-wave (PAW)[33] framework, with a plane-wave kinetic energy cutoff of 450 eV. The exchange–correlation functional was treated within the generalized gradient approximation (GGA) using the Perdew–Burke–Ernzerhof (PBE) functional,[34] supplemented by van der Waals corrections *via* Grimme's DFT-D3 method with Becke–Johnson damping.[35] The Au(111) surface was modeled as a three-layer slab, with the bottom two layers fixed at their bulk positions. A vacuum region of 20 Å was added along the surface normal to eliminate periodic interactions. For isolated adsorbates, a cubic cell with >20 Å of vacuum in all directions was used. The Brillouin zone was sampled using the gamma point. Spin-polarized geometry optimizations were considered converged when the energy change between the electronic steps fell below 10^{-5} eV and the maximum residual force on any atom was less than 0.02 eV $Å^{-1}$. The adsorption energy (E_{ads}) was computed as:

$$E_{\text{ads}} = E_{\text{total}} - E_{\text{slab}} - E_{\text{adsorbate}}$$

where E_{total}, E_{slab}, and $E_{\text{adsorbate}}$ denote the total energy of the adsorption system, clean slab, and the isolated adsorbate in its optimized geometry, respectively. The spin density was defined as the difference between the spin-up and spin-down charge densities and visualized as isosurfaces at an isovalue of 0.001 e $Å^{-3}$.

Conflicts of interest

There are no conflicts to declare.

Data availability

The data supporting the findings of this study are available from the corresponding author upon reasonable request.

Supplementary information (SI): STM, nc-AFM, and synthetic detials for the precursor monomer. See DOI: https://doi.org/10.1039/d6nr00433d.

Acknowledgements

This work was supported by financial support from the National Key Research and Development Program of China (2024YFA1208102), the Quantum Science and Technology-National Science and Technology Major Project (2021ZD0303302), the CAS Project for Young Scientists in Basic Research (YSBR-054), the CAS Strategic Priority Research Program (Grant No. XDB0450201 and XDB36020200), the National Natural Science Foundation of China (No. 22272156, 22373095, 92577202 and 22425206), the Chinese Academy of Sciences (PTYQ2024TD0011), the Anhui Initiative in Quantum Information Technologies (AHY090300) and the New Cornerstone Science Foundation. The computational resources were provided by the Supercomputing Center of the University of Science and Technology of China.

References

1 Y. Zhao, *et al.*, Quantum nanomagnets in on-surface metal-free porphyrin chains, *Nat. Chem.*, 2023, **15**, 53–60.
2 S. Song, *et al.*, On-surface synthesis of graphene nanostructures with π-magnetism, *Chem. Soc. Rev.*, 2021, **50**, 3238–3262.

3 S. Song, *et al.*, Highly entangled polyradical nanographene with coexisting strong correlation and topological frustration, *Nat. Chem.*, 2024, **16**, 938–944.

4 S. Mishra, *et al.*, Observation of fractional edge excitations in nanographene spin chains, *Nature*, 2021, **598**, 287–292.

5 Z. Yuan, *et al.*, Fractional spinon quasiparticles in open-shell triangulene spin-1/2 chains, *J. Am. Chem. Soc.*, 2025, **147**, 5004–5013.

6 C. Zhao, *et al.*, Tunable topological phases in nanographene-based spin-1/2 alternating-exchange Heisenberg chains, *Nat. Nanotechnol.*, 2024, **19**, 1789–1795.

7 C. Zhao, *et al.*, Spin excitations in nanographene-based antiferromagnetic spin-1/2 Heisenberg chains, *Nat. Mater.*, 2025, **24**, 722–727.

8 X. Su, *et al.*, Fabrication of spin-1/2 Heisenberg antiferromagnetic chains via combined on-surface synthesis and reduction for spinon detection, *Nat. Synth.*, 2025, **4**, 694–701.

9 X. Fu, *et al.*, Building spin-1/2 antiferromagnetic Heisenberg chains with diaza-nanographenes, *Nat. Synth.*, 2025, **4**, 684–693.

10 K. Sun, *et al.*, On-surface synthesis of Heisenberg spin-1/2 antiferromagnetic molecular chains, *Sci. Adv.*, 2025, **11**, eads1641.

11 E. Li, *et al.*, Kondo chains of organic radicals on metallic surfaces: A model system of heavy fermion quantum criticality, *J. Am. Chem. Soc.*, 2025, **147**, 46535–46542.

12 W. Zhai, *et al.*, On-surface synthesis and collective spin excitations of antiferro- magnetic spin-1/2 polymer chains, *Nano Res.*, 2025, **18**, 94907415.

13 J. Hieulle, *et al.*, On-surface synthesis and collective spin excitations of a triangulene-based nanostar, *Angew. Chem., Int. Ed.*, 2021, **60**, 25224–25229.

14 D. Li, *et al.*, Frustration-induced many-body degeneracy in spin −1/2 molecular quantum rings, *J. Am. Chem. Soc.*, 2025, **147**, 26208–26217.

15 X. Zhu, *et al.*, Collective magnetism of spin coronoid via on-surface synthesis, *J. Am. Chem. Soc.*, 2025, **147**, 10045–10051.

16 S. Mishra, *et al.*, Synthesis and characterization of π-extended triangulene, *J. Am. Chem. Soc.*, 2019, **141**, 10621–10625.

17 J. Su, *et al.*, Atomically precise bottom-up synthesis of π-extended [5]triangulene, *Sci. Adv.*, 2019, **5**, eaav7717.

18 S. Cheng, *et al.*, On-surface synthesis of triangulene trimers via dehydration reaction, *Nat. Commun.*, 2022, **13**, 1705.

19 S. Mishra, *et al.*, Topological frustration induces unconventional magnetism in a nanographene, *Nat. Nanotechnol.*, 2020, **15**, 22–28.

20 C. Zhao, *et al.*, Tailoring magnetism of graphene nanoflakes via tip-controlled dehydrogenation, *Phys. Rev. Lett.*, 2024, **132**, 046201.

21 A. Vegliante, *et al.*, Tuning the spin interaction in nonplanar organic diradicals through mechanical manipulation, *ACS Nano*, 2024, **18**, 26514–26521.

22 J.-J. Duan, *et al.*, Exploiting structural flexibility for reversible Kondo-state switching in a pure organic radical on Au (111)-submolecular imaging and manipulation, *ACS Nano*, 2025, **19**, 34981–34989.

23 S. Mishra, *et al.*, Nonbenzenoid high-spin polycyclic hydrocarbons generated by atom manipulation, *ACS Nano*, 2022, **16**, 3264–3271.

24 S. Mishra, *et al.*, Bistability between π-diradical open-shell and closed-shell states in indeno[1,2-a]fluorene, *Nat. Chem.*, 2024, **16**, 755–761.

25 K.-H. Chung, *et al.*, Polymorphic porous supramolecular networks mediated by halogen bonds on Ag(111), *Chem. Commun.*, 2011, **47**, 11492–11494.

26 J. K. Yoon, *et al.*, Visualizing Halogen Bonds in Planar Supramolecular Systems, *J. Phys. Chem. C*, 2011, **115**, 2297–2301.

27 R. Gutzler, *et al.*, Halogen bonds in 2D supramolecular self-assembly of organic semiconductors, *Nanoscale*, 2012, **4**, 5965–5971.

28 N. Pavlicek, *et al.*, On-surface generation and imaging of arynes by atomic force microscopy, *Nat. Chem.*, 2015, **7**, 623–628.

29 N. Pavlicek, *et al.*, Generation and characterization of a meta-aryne on Cu and NaCl surfaces, *ACS Nano*, 2017, **11**, 10768–10773.

30 L. Gross, F. Mohn, N. Moll, P. Liljeroth and G. Meyer, The chemical structure of a molecule resolved by atomic force microscopy, *Science*, 2009, **325**, 1110–1114.

31 G. Kresse and J. Furthmüller, Efficiency of *ab initio* total energy calculations for metals and semiconductors using a plane-wave basis set, *Comput. Mater. Sci.*, 1996, **6**, 15–50.

32 G. Kresse and J. Furthmüller, Efficient iterative schemes for *ab initio* total-energy calculations using a plane-wave basis set, *Phys. Rev. B: Condens. Matter Mater. Phys.*, 1996, **54**, 11169–11186.

33 G. Kresse and D. Joubert, From ultrasoft pseudopotentials to the projector augmented-wave method, *Phys. Rev. B: Condens. Matter Mater. Phys.*, 1999, **59**, 1758–1775.

34 J. P. Perdew, K. Burke and M. Ernzerhof, Generalized gradient approximation made simple, *Phys. Rev. Lett.*, 1996, **77**, 3865–3868.

35 S. Grimme, S. Ehrlich and L. Goerigk, Effect of the damping function in dispersion corrected density functional theory, *J. Comput. Chem.*, 2011, **32**, 1456–1465.